Ionics (2016) 22:1159–1166
DOI 10.1007/s11581-016-1648-7

ORIGINAL PAPER

Sintering and electrical conductivity of gadolinia-doped ceria

R. M. Batista [1] · A. M. D. C. Ferreira [2] · E. N. S. Muccillo [1,3]

Received: 15 July 2015 / Revised: 15 December 2015 / Accepted: 11 January 2016 / Published online: 21 January 2016

Abstract Bulk specimens of $Ce_{0.9}Gd_{0.1}O_{2-\delta}$ prepared with powders within a range of specific surface area were sintered in oxidizing, inert, and reducing atmospheres. The aim of this work is to investigate the effects of the sintering atmosphere on the microstructure and grain and grain boundary conductivities of the solid electrolyte. The lattice parameter determined by Rietveld refinement is 0.5420(1) nm, and the microstrain was found negligible in the powder materials. Specimens sintered in the Ar/4 % H_2 mixture display larger average grain sizes independent on the particle size of the starting powders. The grain and grain boundary conductivities of specimens sintered under reducing atmosphere are remarkably lower than those sintered under oxidizing and inert atmospheres. The activation energy (~0.90 eV) for total electrical conductivity remains unchanged with both the initial particle size and the sintering atmosphere.

Keywords Sintering · Ionic conductor · Microstructure · Electrical conductivity

✉ E. N. S. Muccillo
enavarro@usp.br

[1] Energy and Nuclear Research Institute – IPEN, PO Box 11049, São Paulo, SP 05422-970, Brazil

[2] Institute of Chemistry, University of S. Paulo, Av. Prof. Lineu Prestes, 748, São Paulo, SP 05508-000, Brazil

[3] Center of Materials Science and Technology, Av. Prof. Lineu Prestes, 2242, Cidade Universitária, São Paulo, SP 05508-000, Brazil

Introduction

The structural and transport properties of $Ce_{0.9}Gd_{0.1}O_{2-\delta}$, hereafter named GDC, have been extensively investigated, since it possesses attractive properties for application as solid electrolyte in solid oxide fuel cells (SOFCs) operating at intermediate temperatures (500–750 °C) [1, 2]. The relevant property for this application is the high oxide ion conductivity, which results from the compensating mobile oxygen vacancies created by partial cation substitution. This solid electrolyte is known to behave as pure ionic conductor at high oxygen partial pressures ($> 10^{-5}$ atm) and up to moderate temperatures (< 800 °C) [2]. At high temperatures and/or low oxygen partial pressures, loss of oxygen readily occurs in GDC and in other doped ceria, thereby Ce^{4+} reduces to Ce^{3+} according to the defect reaction (written in Kroeger and Vink notation [3]):

$$2Ce_{Ce}^{x} + O_{O}^{x} \leftrightarrow V_{\ddot{O}} + 2Ce_{Ce}^{'} + \frac{1}{2}O_2 \quad (1)$$

with introduction of oxygen vacancies and electrons localized on trivalent cerium forming small polarons [4].

As a consequence of the reduction reaction, an electronic conductivity arises turning the doped ceria mixed ionic and electronic conductors (MIECs) at temperatures above 600 °C [5]. Ceria-based MIECs have potential application as electrode material in SOFCs and for other applications under oxygen lean atmospheres. Dense ceramics are required for most of these applications.

The relatively low sinterability of GDC is well documented, and the main approaches to overcome this problem are the use of nanostructured powders (see for example [6] and references therein), or the introduction of a sintering aid [7–10]. Recently, an increased densification of gadolinia-doped ceria was reported after sintering in reduced oxygen partial pressure

[11]. This effect was attributed to an enhancement of the densification during the early stage of sintering, due to the oxygen vacancies generated by the Ce^{4+} to Ce^{3+} reduction reaction. That work was extended to investigate the effect in GDC prepared with powder with specific surface area of 35 m^2 g^{-1} [12]. It was found that the powder compacts could be sintered in reducing atmosphere (N_2/9 % H_2) to near full density at a relatively low temperature (1050 °C). In a recent work, it was shown that sintering under reducing atmospheres may be catastrophic resulting in severe cracking of GDC bulk specimens, depending on the temperature and oxygen partial pressure [13].

In this work, the effect of sintering in oxidizing, inert, and reducing atmospheres green compacts of GDC prepared with powders with different specific surface areas (from ~7 to ~210 m^2 g^{-1}) was systematically investigated, aiming to contribute to understand the influence of the different atmospheres on the microstructure and ionic conductivity of this solid electrolyte. Special attention was given to the grain and the grain boundary components of the electrical conductivity of GDC.

Experimental

$Ce_{0.9}Gd_{0.1}O_{2-\delta}$ (99.5 %+, Fuel Cell Materials, USA) with different specific surface areas of 7.4, 36.2, and 210 m^2 g^{-1}, hereafter designated S1, S2, and S3, respectively, were used as starting materials without further purification. No additives were employed during processing, and the powders were carefully handled to avoid contamination. X-ray fluorescence analysis showed that the starting powders contain very small amounts of calcium (< 0.4 wt. %).

Disc-shaped specimens with 10-mm diameter and 2–3-mm thickness were prepared by uniaxial pressing with 50 MPa followed by cold isostatic pressing (National Forge Co.) at 70 MPa. Sintering of the green compacts in powder bed was carried out in a resistive furnace (Lindberg Tube Furnace) with 10 °C min^{-1} heating rate up to 1250 °C for 2 h under air, argon, nitrogen, and argon-4 % hydrogen mixture atmospheres. The purity of these gases was 99.99 %, and the flow rate was 2 cm^3 min^{-1}. The sintering profile was chosen to result in specimens with relative densities higher than 92 %.

X-ray diffraction analysis (XRD) (Bruker-AXS, D8 Advance) was performed on powders and sintered specimens in the 23–73° 2θ range with 0.04° step size and 5-s counting time with Ni-filtered Cu K_α radiation. Instrumental broadening and peak asymmetry were determined with CeO_2 standard (particle size ~10 μm) and fixed during refinements. The XRD patterns were used for crystallite size (d_{XRD}), lattice parameter (a), and microstrain (e) determination with Rietveld refinement by GSAS. The peak profiles were modeled using a modified pseudo-Voigt function (function #2). Density measurements were performed by measuring the specimen dimensions and mass. Polished (diamond pastes of 6 and 1 μm) and thermally etched (80 °C below the sintering temperature) surfaces of sintered specimens were observed in a field emission scanning electron microscope (FESEM) (FEI, Inspect F50). The average grain size (G) was determined by the intercept method using the ImageJ software. Raman spectroscopy measurements (Renishaw inVia Raman microscope) were carried out in the phonon (200–800 cm^{-1}) and electronic (1800–2300 cm^{-1}) ranges looking for possible Ce^{3+} formation during sintering. For these measurements, a laser with 633-nm wavelength and 45-mW power was set. These room temperature spectra are mostly related to the surface chemistry of the studied specimens. Then, possible formation of Ce^{3+} in the bulk of sintered materials was investigated by electron paramagnetic resonance (EPR) measurements in a X band instrument (Bruker, EMX, 9.5 GHz). All analyses were performed at room temperature, in standard Wilmad quartz tubes (4 mm, internal diameter), on powder as well as on sintered and finely ground specimens, using 20.07 mW of microwave power and 100 kHz of modulated field. α,α′-Diphenyl-β-picrylhydrazyl (DPPH) was used for frequency calibration. Usually, 1.12 to 4.48 × 10^2 gain and 15-G modulation amplitude were used when registering the spectra and double integration to compare the intensity of the signals. Electrical conductivity measurements were carried out on metalized (silver paste followed by curing at 400 °C) specimens with an impedance analyzer (HP 4192A) in the 5 Hz–13 MHz and 150–330 °C frequency and temperature ranges, respectively, with 100 mV of applied voltage. All impedance spectroscopy measurements were carried out in air (pO_2 = 0.21 atm). Preliminary results on densification and electrical conductivity of specimen S2 may be found elsewhere [14].

Results and discussion

Figure 1 shows, as an example, the X-ray diffraction pattern of one of the powders (S2) with the Rietveld refinement. Small marks in the bottom of this figure are the Bragg angular positions of reflections of the cubic phase (*Fm-3m*, space group). The value of chi-square was 1.109.

The experimental pattern corresponds to the characteristic cubic fluorite-like phase of ceria. The broadening of the diffraction peaks is related to the small crystallite size of this powder. Similar results were obtained for other powders (S1 and S3).

Table 1 lists values of the crystallite size (d_{XRD}) and microstrain (e) for the starting materials.

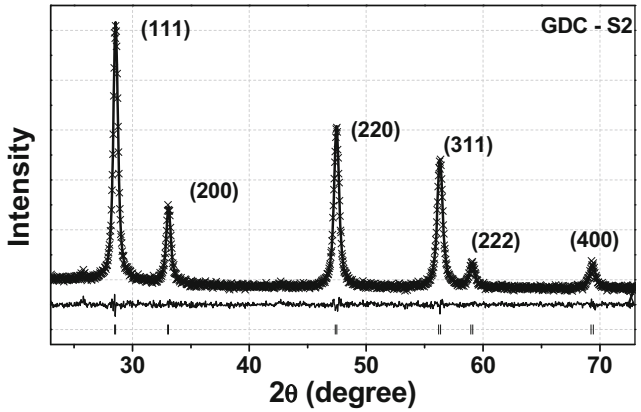

Fig. 1 Example of the Rietveld refinement for S2 powder. XRD data (*crosses*), model (*line*), residues (*line* below the XRD pattern), and angular position of the specific reflections of the cubic fluorite-like phase (*small marks*)

The crystallite sizes correlate with those obtained from transmission electron microscopy (not shown here) revealing that the starting materials consist of single crystalline nanoparticles, within the resolution limits and experimental precision of the diverse techniques. The microstrain is found negligible for all powders, although a net tendency to increase with decreasing the particle size may be noticed.

The lattice parameter and the theoretical density determined after Rietveld refinements are 0.5420(1) nm and 7.2146(9) g cm^{-3}, respectively. These figures are in general agreement with literature data [15, 16].

The relative green density of specimens prepared with these nanopowders is a decreasing function of the specific surface area: 60 % (S1), 48 % (S2), and 40 % (S3), as expected. The relative density of specimens sintered at several atmospheres is summarized in Table 2.

No substantial changes in the sintered density (< 3 %) are found by varying the sintering atmosphere. Then, from thermodynamic considerations, the interactions (including solubilities) of gaseous species with the ceria matrix and the dopant are similar. Slightly lower values of density are obtained for specimens prepared with powder S1 independent on the atmosphere, evidencing a relatively small effect of the particle size upon sintering. Specimens sintered in the Ar/4 % H_2 mixture exhibit the lowest values of density. This effect seems to be independent on the initial particle size of the powder.

The effects of the sintering atmosphere on the microstructure of GDC are illustrated in Figs. 2 and 3.

Table 1 Values of crystallite size (d_{XRD}) and microstrain (e) of as-received materials

Material	d_{XRD} (nm)	e ($\times 10^4$ %)
S1	72 (5)	0
S2	14.9 (3)	0.3
S3	4.2 (2)	5

Table 2 Values of relative density of $Ce_{0.9}Gd_{0.1}O_{2-\delta}$ specimens sintered under air, nitrogen, argon, and the mixture of Ar-4 % H_2 at 1250 °C for 2 h

Atmosphere	Relative density (%)		
	S1	S2	S3
Air	93.2	95.6	96.8
N_2	95.4	96.5	95.1
Ar	95.0	96.9	96.9
Ar/4 % H_2	92.1	92.3	93.8

Figure 2 shows representative FESEM micrographs of specimens prepared with powder S3 sintered in oxidizing (a) and inert (b and c) atmospheres. These specimens exhibit similar features, such as polyhedral grains in the submicrometer range and low porosity more often confined at grain boundaries and triple grain junctions.

Slightly larger average grain size is observed for specimens sintered in nitrogen (c) compared to argon (b), revealing marginal differences among the interactions of theses gaseous species with GDC.

The FESEM micrographs of specimens sintered in the Ar/4 % H_2 mixture are shown in Fig. 3 for specimens prepared with powders S1 (a), S2 (b), and S3 (c). The large grain size of these specimens is worth noting compared to those sintered in inert and oxidizing atmospheres (Fig. 2).

Surprisingly, no significant difference is observed in the microstructure of sintered specimens as a function of the initial particle size. This means that GDC powder with very small particle size should exhibit an accelerated grain growth. The large grain size (in the micrometer range) in these specimens is accompanied by both intergranular and intragranular pores. Moreover, intergranular cracks were observed in general agreement with recent observations and may be responsible for reducing the sintered density [13, 17].

The kinetics of grain growth in GDC sintered in reducing atmosphere has been recently studied [11]. The enhanced densification during the early stage sintering was attributed to the formation of oxygen vacancies due to reduction of Ce^{4+} to Ce^{3+}, which assists the diffusion of ions through the lattice.

These findings emphasize that the effects of the initial particle size play a minor role in the microstructure development of GDC, at least in the particle size range investigated in this work.

Table 3 lists values of the average grain size determined by the intercept method for all investigated specimens.

The average grain size of specimens sintered in reducing atmosphere is approximately four times larger than that of specimens sintered in other atmospheres. This effect may be related to an increase of the oxygen vacancy concentration due to the reduction reaction according to Eq. (1).

The structure of the diverse specimens was analyzed by Raman spectroscopy after sintering. Figure 4 shows Raman spectra of specimens prepared with S3 powder and sintered in

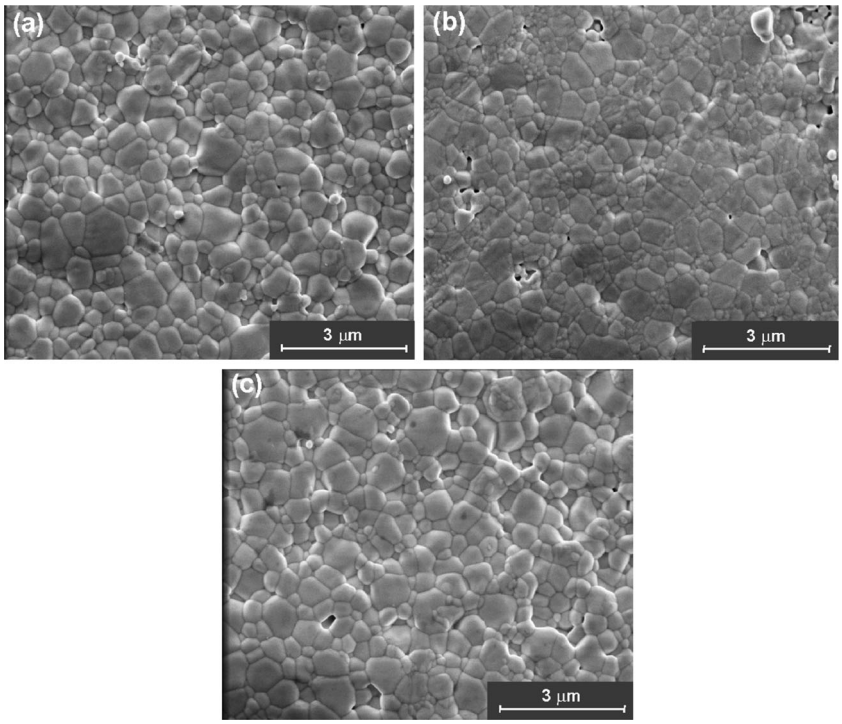

Fig. 2 FESEM micrographs of GDC prepared with S3 powder and sintered in **a** air, **b** argon, and **c** nitrogen at 1250 °C for 2 h

oxidant and oxygen-lean atmospheres. In the 200–800 cm^{-1} range (Fig. 4a), the spectra display a high-intensity band centered at 460 cm^{-1} typical of the triple degenerated F_{2g} mode of the fluorite lattice of ceria and assigned to a symmetric breathing mode of Ce-O8 vibrational unit. The asymmetry of this band testifies the formation of solid solution between cerium and gadolinium in the lattice. In addition, two low-intensity bands in the ~500–~650 cm^{-1} range associated to extrinsic oxygen vacancies are observed [18].

Figure 4b shows the electronic Raman spectrum of the specimen prepared with S3 powder sintered in the Ar/4 % H_2 mixture. No Raman band was detected at 2165 cm^{-1}, where a low-intensity band due to the electronic transition $^2F_{7/2} \rightarrow {}^2F_{5/2}$ of Ce_2O_3 is expected to occur [19]. Similar

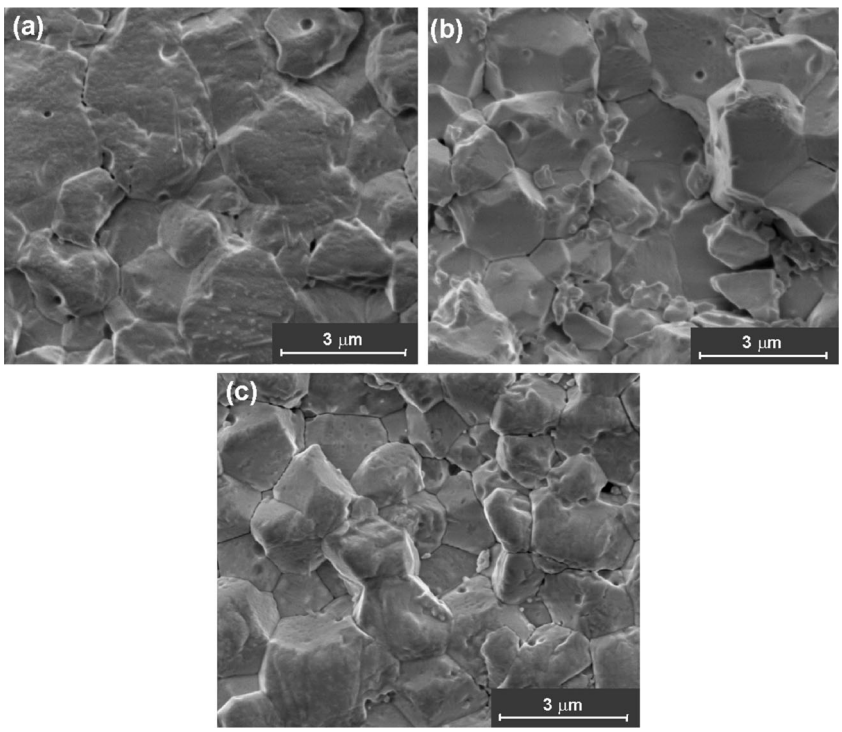

Fig. 3 FESEM micrographs of GDC prepared with powders **a** S1, **b** S2, and **c** S3 and sintered at 1250 °C for 2 h in Ar/4 % H_2

Table 3 Values of average grain size of GDC prepared with powders S1, S2, and S3 and sintered at several atmospheres at 1250 °C/ 2 h

Atmosphere	Average grain size (μm)		
	S1	S2	S3
Air	0.59	0.61	0.62
N_2	0.73	0.71	0.65
Ar	0.67	0.67	0.63
Ar/4 % H_2	2.70	2.41	2.22

results were obtained for other specimens sintered in the several atmospheres. These Raman spectroscopy results indicate the absence of Ce^{3+} on the surface of sintered specimens.

Nevertheless, a visual inspection of specimens prepared with powder S3 and sintered in oxygen-lean atmosphere evidenced a slight change of color from white-cream to gray-green suggesting some degree of valence change of cerium ions. Then, the same specimens were finely ground and analyzed by electron paramagnetic resonance for possible detection of Ce^{3+} in the bulk of the compacts.

It is generally known that Ce^{4+} ions are inactive or silent in EPR for no unpaired electrons, in contrast to Ce^{3+}, with

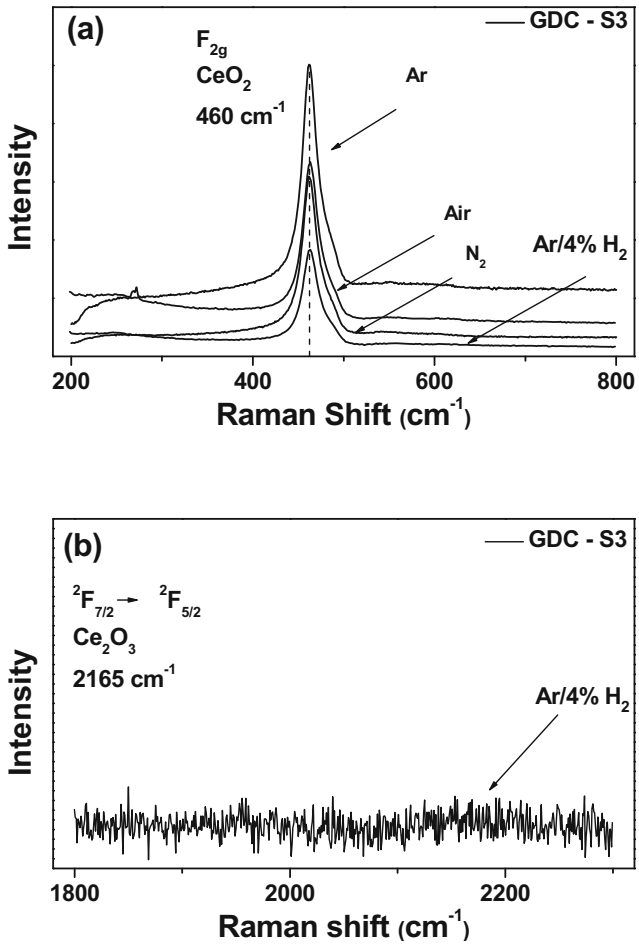

Fig. 4 Raman spectra of specimens prepared with S3 powder and sintered at several atmospheres: **a** phonon and **b** electronic ranges

configuration [Xe] $4f^1$. Previous results on ceria and cerium hydroxide have shown two main *si*gnals: A ($g_\perp$= 1.967; $g_\parallel$= 1.947) and D ($g_\perp$= 1.967; $g_\parallel$= 1.940), respectively. The intensity of signal D was found to be much higher than that of signal A, but decreased steadily upon heating treatments at increasing temperatures and finally disappeared at approximately 800 °C [20]. Similar results were obtained by EPR measurements in specimens treated under vacuum and reducing atmospheres [21].

The interpretation of EPR signals in doped ceria is not straightforward as in undoped cerium oxide, because the partial substitution of cerium ions by aliovalent ions induces a substantial broadening of these signals along with reduction of their intensities. In the case of $(CeO_2)_{1-x}(BiO_{1.5})_x$ with $x = 0.17$ and 0.50 solid solutions, the intensity of EPR signals was found to decrease drastically with increasing dopant content [22]. The EPR signals of $Ce_{1-x}RE_xO_{2-\delta}$ (RE = Eu, Tb) broadened with both dopants, and the g values shifted to ≃2.0. These features were attributed to Ce^{3+} occupying the lattice sites of lower symmetry. Increased broadening of EPR signals and g values around 2.0 were also evidenced in $Ce_{1-x}Nd_xO_{2-\delta}$ ($0.05 \le x \le 0.40$) [23] and $Ce_{1-x}Gd_xO_{2-x/2}$ (x = 0.1; 0.2) [24]. The broadening of the EPR signal has been found also to occur in other gadolinium compounds such as in double-doped ceria [25], in the glass $x.Gd_2O_3$ + (1-x) (La_2O_3)-Al_2O_3-B_2O_3-Si_2O_3-GeO_2 [26], and in the superconductor $GdBa_2Cu_3O_y$ [27]. Those independent studies have suggested that the broadening effect is due to a magnetic coupling among Gd^{3+} ions.

In this work, the dopant concentration is the same for all specimens. Then, any change in the EPR signal of GDC specimens sintered in different atmospheres is assigned to an interference caused by the presence of Ce^{3+} that might be formed in the bulk. The exact nature of that interference is outside the scope of this paper. The EPR spectra of the starting powders were first recorded and subtracted from those of the sample holder (blank). The corresponding result for powder S3 is indicated by an asterisk in Fig. 5a. The near absent EPR signal in this spectrum reveals that the fraction of Ce^{3+} in the starting materials is negligible. Similar results were obtained for other powders.

The EPR spectra of specimens prepared with the S3 powder and sintered in air, nitrogen, and argon atmospheres are also shown in Fig. 5a. A broad band is observed for all specimens. For materials sintered in the Ar/4 % H_2 mixture (Fig. 5b), the relative intensity of that band is higher than that for other atmospheres (the EPR signal for the specimen sintered in Ar is reproduced in Fig. 5b for comparison purposes). In all these spectra, g is ≃2.0. A low-intensity EPR signal for the air-sintered specimen is worth noting, revealing a non-negligible reduction of Ce^{4+} at the sintering temperature even in an oxidizing atmosphere. Similar results were obtained for specimens prepared with powders S1 and S2 exposed to

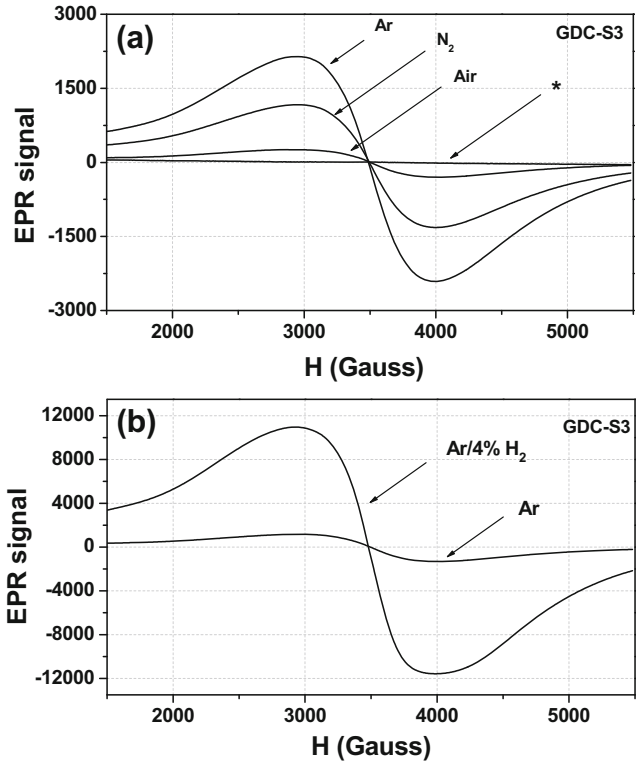

Fig. 5 Room temperature first derivative EPR spectra of S3 powders **a**, starting powder (*asterisk*), and after sintering in air, N_2, and Ar and **b** after sintering in Ar and Ar/4 % H_2

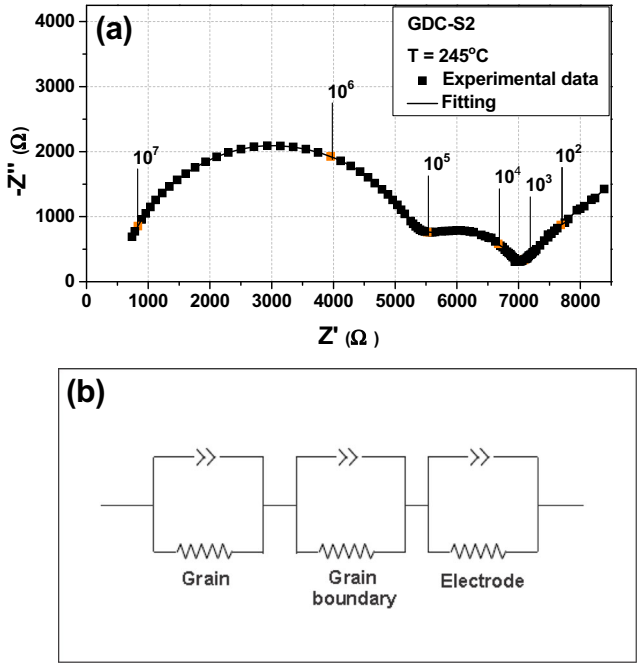

Fig. 6 **a** Impedance spectroscopy diagram at 245 °C of the sintered specimen prepared with powder S2 and **b** equivalent circuit. Numbers stand for the frequency (Hz)

the same sintering profile. The higher intensity of the EPR signal of the specimen sintered in the Ar/4 % H_2 atmosphere is remarkable, suggesting that a significant fraction of Ce^{3+} has been formed even for the mild sintering profile used in this work. To avoid any doubt concerning the origin of the EPR signal in our specimens, after the measurements, the powder specimens were stored at ambient atmosphere for few weeks and then measured again. As a result, no EPR signal was detected independent on either the starting powder or the sintering atmosphere.

Figure 6a shows an impedance spectroscopy diagram recorded at 245 °C for GDC specimen sintered in air prepared with powder S2. These measurements were carried out at a fixed time interval after sintering, due to the oxidation reaction of Ce^{3+} to Ce^{4+}.

In the temperature and frequency ranges of measurements, the impedance diagrams of all sintered specimens consist in three main contributions due to the capacitive and resistive effects of the bulk (high frequency), grain boundary (intermediate frequency), and electrode (low frequency), as exemplified in Fig. 6a. The shape of impedance diagrams does not depend on the particle size and sintering atmosphere. Thus, in spite of the reduction reaction that was observed to occur in reducing atmospheres, the electrical conductivity of GDC remained predominantly ionic in the temperature range of measurements.

The fitting of the impedance diagrams was carried out using the equivalent electric circuit shown in Fig. 6b. The analysis of the diagrams allowed for obtaining the grain and grain boundary conductivities of GDC (Fig. 7). The specific grain boundary conductivity was calculated by normalizing the experimental data for the average grain size (Table 3).

The behavior of the grain conductivity (Fig. 7a) may be represented by a single straight line giving an activation energy value of 0.79 eV. There is no apparent difference in the conductivity values of specimens sintered in oxidizing and inert atmospheres. In contrast, the specimens sintered in reducing atmosphere exhibit lower (about half order of magnitude) grain conductivity. This effect is attributed to the reduction of cerium ions inside the grains and the consequent loss of stoichiometry of the solid electrolyte.

The specific grain boundary conductivity (Fig. 7b) of air-sintered specimens (full symbols) did not change with the particle size. On the other hand, for specimens sintered in inert atmospheres (half-full and half-empty symbols), a small increase of the grain boundary conductivity is observed for specimens prepared with powders S1 and S2 compared to air-sintered specimens. This effect may be assigned to the beneficial effect of oxygen vacancy creation due to reduction reaction (see Eq. 1). Specimens prepared with powder S3 sintered in inert atmospheres, in contrast, exhibit lower grain boundary conductivity. In this case, intergranular cracks may account for that result. All specimens sintered in the Ar/4 % H_2 mixture display the lowest values of specific grain boundary conductivity (empty symbols) among the investigated materials. These results along with those

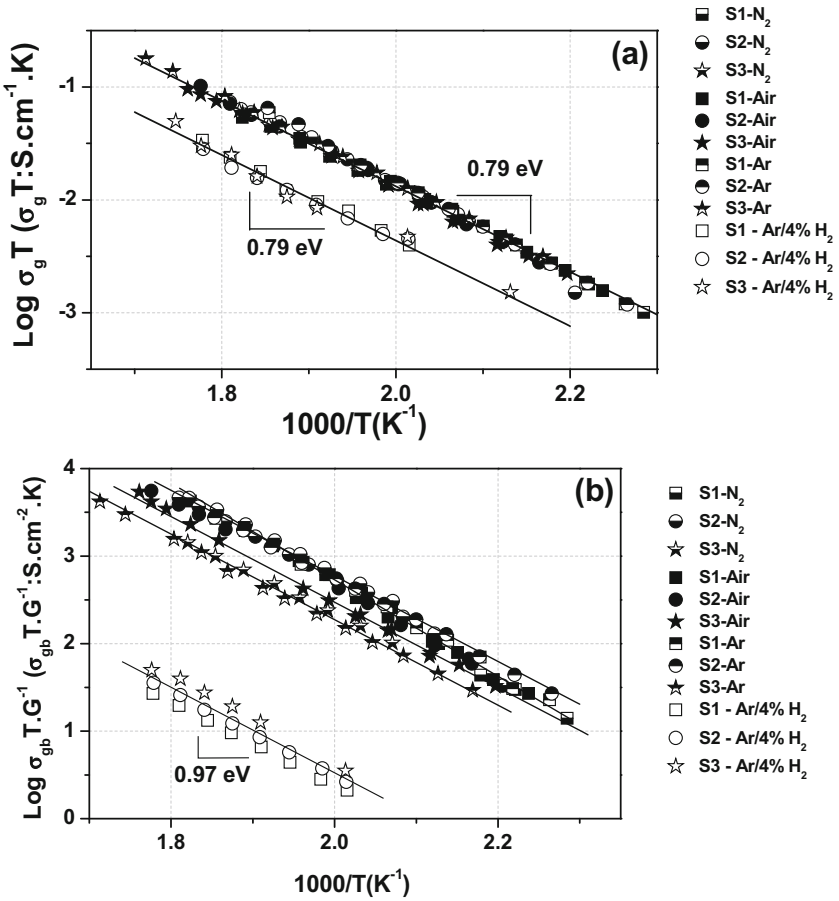

Fig. 7 Arrhenius plots of the **a** grain and **b** specific grain boundary conductivity of GDC-sintered specimens

for the grain conductivity (Fig. 7a) suggest that the consequences of the reduction reaction are severe for both the grain and the grain boundaries. The activation energy for specific grain boundary conduction is 0.97 eV for compacts prepared with powders S2 and S3 and 1.0 eV for powder S1.

The Arrhenius plots of the total electrical conductivity are shown in Fig. 8.

The total electrical conductivity of GDC is approximately independent on the initial particle size of the powder. Remarkable decrease of the total conductivity (about one order of magnitude) was obtained for specimens sintered in reducing atmosphere. The presence of microcracks, pores, and Ce_2O_3 may account for this effect. The activation energy for electrical conductivity is 0.90 eV.

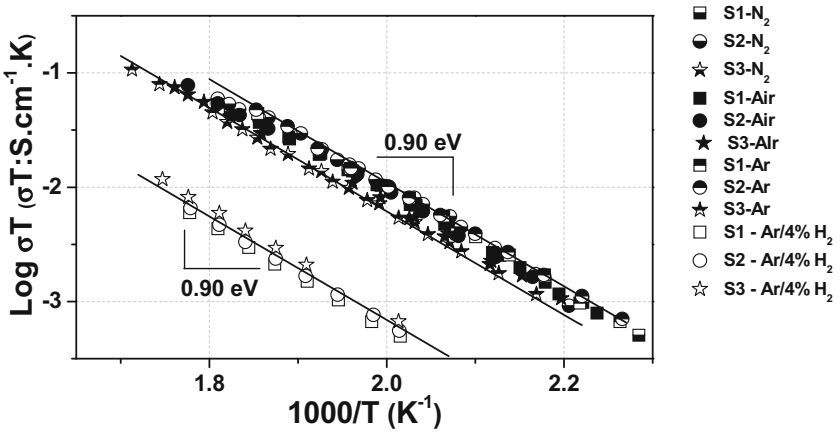

Fig. 8 Arrhenius plots of the total electrical conductivity of GDC-sintered specimens

Conclusion

$Ce_{0.9}Gd_{0.1}O_{2-\delta}$ within a broad range of specific surface area was sintered to high density (>92 % of the theoretical value) in oxidizing, inert, and reducing atmospheres. Electron paramagnetic resonance allowed for detecting the effect of Ce^{3+} formed in the bulk of the specimens. The oxidation of Ce_2O_3 readily occurs when specimens are exposed to ambient air. The average grain size of specimens sintered in reducing atmosphere is about four times larger than that of the specimens sintered in other atmospheres. The grain conductivity of GDC sintered in Ar/4 % H_2 mixture is about half-order of magnitude lower than that of specimens sintered in other atmospheres.

Acknowledgments The authors gratefully acknowledge the financial supports from FAPESP (#2013/07296-2), CNPq (#573636/2008-7), and CNEN; the Laboratory of Molecular Spectroscopy of the University of S. Paulo for the Raman experiments; and Prof. M. Kleitz for the comments on the manuscript. R. M. Batista acknowledges CAPES for the scholarship.

References

1. Minh NQ (1993) Ceramic fuel cells. J Am Ceram Soc 76:63–88. doi:10.1111/j.1151-2916.1993
2. Steel BCH (2000) Appraisal of $Ce_{1-y}Gd_yO_{2-y/2}$ electrolytes for IT-SOFC operation at 500°C. Solid State Ionics 129:95–110. doi:10.1016/S0167-2738(99)00319-7
3. Kroeger FA, Vink HJ (1956) In: Seitz F, Turnbull D (eds) Relations between the concentrations of imperfections in crystalline solids. Solid State Physics v 3 Academic Press, New York, p. 307
4. Tuller HL, Nowick AS (1977) Small polaron electron transport in reduced CeO_2 single crystals. J Phys Chem Solids 38:859–867. doi:10.1016/0022-3697(77)90124-X
5. Tuller HL, Nowick AS (1975) Doped ceria as a solid electrolyte. J Electrochem Soc 122:255–259. doi:10.1149/1.2134190
6. Shao Z, Zhou W, Zhu Z (2012) Advanced synthesis of materials for intermediate temperature solid oxide fuel cells. Progr Mater Sci 57:804–874. doi:10.1016/j.pmatsci.2011.08.002
7. Dikmen S (2010) Effect of co-doping with Sm^{3+}, Bi^{3+}, La^{3+} and Nd^{3+} on the electrochemical properties of hydrothermally prepared gadolinium-doped ceria. J Alloy Compd 491:106–112. doi:10.1016/j.jallcom.2009.11006
8. Gil V, Moure C, Durán P, Tartaj J (2007) Low temperature densification and grain growth of Bi_2O_3-doped-ceria gadolinia ceramics. Solid State Ionics 178:359–365. doi:10.1016/j.ssi.2007.02.002
9. Dong YC, Hampshire S, Zhou JE, Meng GY (2011) Synthesis and sintering of Gd-doped CeO_2 electrolytes with and without 1at.% CuO dopping for solid oxide fuel cell applications. Int J Hydrog Energy 36:5054–5066. doi:10.1016/j.ijhydene.2011.01.030
10. Horovistiz AL, Muccillo ENS (2012) Microstructural and electrical characterizations of chemically prepared $Ce_{0.8}Gd_{0.2-x}(Ag, Sr)_xO_{1.9}$ ($0 \le x \le 0.02$). Solid State Ionics 225:428–431. doi:10.1016/j.ssi.2012.05.027
11. He Z, Yuan H, Glasscock JA, Chatzichristodoulou C, Phair JW, Kaiser A, Ramousse S (2010) Densification and grain growth during early-stage sintering of $Ce_{0.9}Gd_{0.1}O_{1.95-\delta}$ in a reducing atmosphere. Acta Mater 58:3860–3866. doi:10.1016/j.actamat.2010.03.046
12. Esposito V, Ni DW, He Z, Zhang W, Prasad AS, Glasscock JA, Chatzichristodoulou C, Ramousse S, Kaiser A (2013) Enhanced mass diffusion phenomena in highly defective doped ceria. Acta Mater 61:6290–6300. doi:10.1016/j.actamat.2013.07.012
13. Kim KJ, Choi GM (2015) Phase stability and oxygen non-stoichiometry of Gd-doped ceria during sintering in reducing atmosphere. J Electroceram. doi:10.1007/s10832-015-9993-8
14. Batista RM, Muccillo ENS (2014) Effect of sintering atmosphere and particle size on the ionic conductivity of gadolinia-doped ceria. ECS Trans 61:361–367. doi:10.1149/06101.0361ecst
15. Mogensen M, Sammes NM, Tompsett GA (2000) Physical, chemical and electrochemical properties of pure and doped ceria. Solid State Ionics 129:63–94. doi:10.1016/S0167-2738(99)00318-5
16. Kharton VV, Figueiredo FM, Navarro L, Naumovich EN, Kovalevsky AV, Yaremchenko AA, Viskup AP, Carneiro A, Marques FMB, Frade JR (2001) Ceria-based materials for solid oxide fuel cells. J Mater Sci 36:1105–1117. doi:10.1023/A:1004817506146
17. Mi DW, Glasscock JA, Pons A, Zhang W, Prasad A, Sanna S, Pryds N, Esposito V (2014) Densification of highly defective ceria by high temperature controlled re-oxidation. J Electrochem Soc 161:F3072–F3078. doi:10.1149/2.0121411jes
18. McBride BJR, Hass KC, Poindexter BD, Weber WH (1994) Raman X-ray studies of $Ce_{1-x}RE_xO_{2-y}$, where RE = La, Pr, Nd, Eu, Gd and Tb. J Appl Phys 76:2435–2441. doi:10.1063/1.357593
19. Otake T, Yugami H, Saito N, Kawamura K, Kawada T, Mizusaki J (2000) Ce^{3+} concentration in ZrO_2-CeO_2-Y_2O_3 studied by electronic Raman spectroscopy. Solid State Ionics 135:663–667. doi:10.1016/S0167-2738(00)00428-8
20. Abi-aad E, Bechara R, Grimblot J, Aboukais A (1993) Preparation and characterization of CeO_2 under an oxidizing atmosphere. Thermal Analysis, XPS, and EPR Study. Chem Mater 5:793–797. doi:10.1021/cm00030a013
21. Fierro JLG, Soria J, Sanz J, Rojo JM (1987) Induced changes in ceria by thermal treatments under vacuum or hydrogen. J Solid State Chem 66:154–162. doi:10.1016/0022-4596(87)90230-1
22. Li G, Mao Y, Li L, Feng S, Wang M, Yao X (1999) Solid solubility and transport properties of nanocrystalline $(CeO_2)_{1-x}(BiO_{1.5})_x$ by hydrothermal conditions. Chem Mater 11:1259–1266. doi:10.1021/cm9806735
23. Li L, Lin X (2001) Solid solubility and transport properties of $Ce_{1-x}Nd_xO_{2-\delta}$ nanocrystalline solid solutions by a sol-gel route. J Mater Res 16:3207–3213. doi:10.1557/JMR.2001.0442
24. Sin A, Yu D, Zaopo A, Aricó AS, Gullo L, La Rosa D, Siracusano S, Antonucci V, Oliva C, Ballabio O (2004) Preparation and sintering of $Ce_{1-x}Gd_xO_{2-x/2}$ nanopowders and their electrochemical and EPR characterization. Solid State Ionics 175:361–366. doi:10.1016/j.ssi.2004.03.034
25. Rakhmatullin RM, Aminov LK, Kurkin IN, Boetvher R, Poppl A, Ávila-Paredes H, Kim S, Sen S (2009) Electron paramagnetic resonance linewidth narrowing of Gd^{3+} ions in Y-doped ceria nanocrystals with decreasing crystallite size. J Chem Phys 131:124515. doi:10.1063/1.3225487
26. Kliava J, Malakhovskii A, Edelman I, Potseluyko A, Petrakovskaya E, Melnikova S, Zarubina T, Petrovxkii G, Bruckental Y, Yeshurun Y (2005) Unusual magnetic transitions and nature of magnetic resonance spectra in oxide glasses containing gadolinium. Phys Rev B 71:104406. doi:10.1103/PhysRevB71.104406
27. Nakamura F, Senoh K, Tamura T, Ochiai Y, Narahara Y (1989) Magnetic interactions in $GdBa_2Cu_3O_y$. Physica C 162:1287–1288. doi:10.1016/0921-4534(89)90696-5